Nano Research

Open Access

Research Article

Magnetic tuning of optical anisotropy in 2D materials: Insights from antiferromagnetic-TMDC interfaces

Miaoxia Gao[1,2], Xing Xie[1,2], Junying Chen[1,2], Junnan Ding[1,2], Fangping Ouyang[1,3], Zongwen Liu[4,5], Jian-Tao Wang[6,7,8], Jun He[1,2], and Yanping Liu[1,2] ✉

[1] *Institute of Quantum Physics, School of Physics, Central South University, Changsha 410083, China*
[2] *State Key Laboratory of Precision Manufacturing for Extreme Service Performance, Central South University, Changsha 410083, China*
[3] *School of Physics and Technology, State Key Laboratory of Chemistry and Utilization of Carbon Based Energy Resources, Xinjiang University, Urumqi 830046, China*
[4] *School of Chemical and Biomolecular Engineering, The University of Sydney, NSW 2006, Australia*
[5] *The University of Sydney Nano Institute, The University of Sydney, NSW 2006, Australia*
[6] *Beijing National Laboratory for Condensed Matter Physics, Institute of Physics, Chinese Academy of Sciences, Beijing 100190, China*
[7] *School of Physical Sciences, University of Chinese Academy of Sciences, Beijing 100049, China*
[8] *Songshan Lake Materials Laboratory, Dongguan 523808, China*

Cite this article: *Nano Research*, **2025**, *18*, 94907111. https://doi.org/10.26599/NR.2025.94907111

ABSTRACT: Atomically thin two-dimensional (2D) magnetic materials offer unique opportunities to enhance interactions between electron spin, charge, and lattice, leading to novel physical properties at low-dimensional scales. While extensive research has explored how breaking three-fold (C_3) rotational symmetry in transition metal dichalcogenides (TMDC) can induce optical anisotropy at heterointerfaces, the role of magnetism in modulating these anisotropic optical properties remains underexplored. Here, we engineer an antiferromagnet/semiconductor heterostructure by coupling isotropic $MoWSe_2$ with the low-symmetric antiferromagnet $NiPS_3$, introducing in-plane anisotropy in the $MoWSe_2$ alloy. Low-temperature photoluminescence (PL) measurements reveal a pronounced linear polarization-dependent exciton emission intensity at the $MoWSe_2/NiPS_3$ interface, with anisotropy ratios of 1.09 and 1.07 for charged and neutral excitons, respectively. Furthermore, applying an out-of-plane magnetic field results in a dramatic rotation of the exciton polarization direction by up to 90° at 9 T, significantly exceeding the previously reported maximum deflection of around 27°. This pronounced polarization rotation is not solely attributed to valley coherence, indicating a strong influence of the magnetic order in $NiPS_3$. These findings provide new insights into the role of magnetic ordering in tuning optical anisotropy in 2D materials, paving the way for the development of advanced polarization-sensitive optoelectronic and magneto-optic devices.

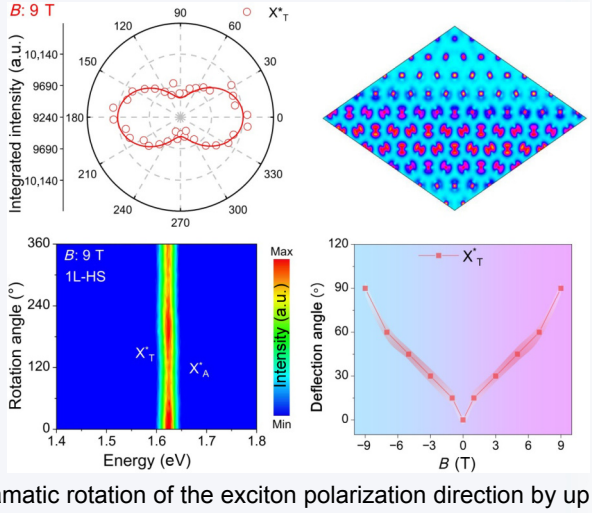

KEYWORDS: transition metal dichalcogenides (TMDC), optical anisotropy, symmetry engineering, antiferromagnetic $NiPS_3$

1 Introduction

The breaking of inversion, rotational, time-reversal, and gauge symmetries in low-dimensional transition metal dichalcogenides opens up new avenues for exploring quantum phenomena, such as Hall effects, spin–orbit interactions, piezoelectricity, and superconductivity [1–7]. While techniques like strain engineering, electric fields, and phase transitions have been used to break rotational symmetry, heterointerface coupling in van der Waals (vdW) heterostructures [8]—formed by stacking materials with different symmetries—has shown asymmetric optical behaviors at the interfaces of heterojunctions, as observed in WS_2/ReS_2, ReS_2/WSe_2, and MoS_2/BP systems [9–15]. The recent discovery of two-dimensional (2D) vdW magnets with intrinsic magnetic ordering offers a promising platform to further explore these effects

Received: September 4, 2024; **Revised:** October 23, 2024
Accepted: November 4, 2024

✉Address correspondence to liuyanping@csu.edu.cn

[16–19]. However, despite extensive studies on anisotropy in transition metal dichalcogenides (TMDC) through heterointerface engineering, the influence of magnetism on their optical properties remains poorly understood. To address this gap, it is crucial to explore new magnetic layered materials with intrinsically low-symmetry crystal structures, such as orthorhombic, monoclinic, and triclinic 2D materials that exhibit pronounced anisotropic properties. In particular, $NiPS_3$, a layered antiferromagnetic insulator with a monoclinic structure (C_{2h} point group), exhibits strong anisotropic characteristics [3, 20–22], while $MoWSe_2$, a TMDC alloy with hexagonal C_3 rotational symmetry, typically shows in-plane isotropy [23, 24].

In this study, we report on the fabrication of a vdW heterostructure comprising the antiferromagnetic insulator $NiPS_3$ and the semiconductor TMDC alloy $MoWSe_2$. Our results demonstrate that the interface effects in this heterostructure induce optical anisotropy in the initially isotropic $MoWSe_2$ due to symmetry disruption caused by the $NiPS_3$ layer. Angular-resolved polarized photoluminescence (PL) and Raman spectroscopy reveal a dumbbell-shaped pattern, indicating the emergence of optical anisotropic features in the $MoWSe_2/NiPS_3$ heterostructure. Furthermore, we show that the optical anisotropy can be effectively modulated by applying an external magnetic field, leading to a deflection angle of polarized excitons up to 90° at 9 T. This significant deviation primarily arises from valley coherence and antiferromagnetic ordering in $NiPS_3$. Additionally, the polarization direction of the A_{1g} vibrational mode (247.7 cm^{-1}) in $MoWSe_2$ shifts by 35° at 9 T and by 34° at −9 T. Density functional theory (DFT) calculations further confirm that the anisotropic optical properties originate from the non-uniform charge density distribution near the conduction band edge in $MoWSe_2$ layers. The C_3 rotational symmetry of $MoWSe_2$ is broken by the C_2 symmetry of $NiPS_3$, resulting in polarization-resolved anisotropic properties at the heterojunction interface. These findings advance our understanding of magneto-optical coupling in antiferromagnetic materials and open new possibilities for developing polarization-sensitive optoelectronic and photonic devices with enhanced functionalities and tunable properties [7, 18, 25–31].

2 Results and discussions

2.1 Optical characterization of $MoWSe_2/NiPS_3$ heterojunction

$MoWSe_2$ monolayers and $NiPS_3$ sheets are prepared by mechanical cleavage of corresponding bulk single crystals (HQ graphene) on SiO_2/Si substrates. Here, we employ a dry transfer method to vertically stack $MoWSe_2$ onto the $NiPS_3$ flakes, forming the $MoWSe_2/NiPS_3$ heterostructure. As depicted in the schematic crystal structure in Fig. 1(a), monolayer $MoWSe_2$ exhibits threefold rotational symmetry, whereas $NiPS_3$ demonstrates twofold rotational symmetry [32]. Figure 1(b) shows an optical micrograph of the sample with a scale bar of 40 μm, where the regions of monolayer (1L) and bilayer (2L) $MoWSe_2$, as well as few-layer $NiPS_3$, are outlined by white and yellow dashed lines, respectively. The absence of cracks or folds in the overlapping regions highlights the high quality of the heterostructure, which is further corroborated by the PL mappings in Fig. 1(c). We perform spatially resolved PL measurements over the 10 μm × 10 μm area marked by the red dashed box in Fig. 1(b). Distinct boundaries between different regions are indicated by variations in PL intensity, with monolayer $MoWSe_2$ exhibiting the strongest luminescence. The PL spectra in Fig. 1(d), recorded at room temperature for 1L-$MoWSe_2$, 2L-$MoWSe_2$, 1L-$MoWSe_2/NiPS_3$ (1L-HS), and 2L-$MoWSe_2/NiPS_3$ (2L-HS), reveal a significant quenching [33] of PL signals in 1L-HS compared to 1L-$MoWSe_2$. Theoretical calculations suggest that $MoWSe_2$ and $NiPS_3$ form a type-II staggered band alignment, with the conduction band minimum in $NiPS_3$ and the valence band

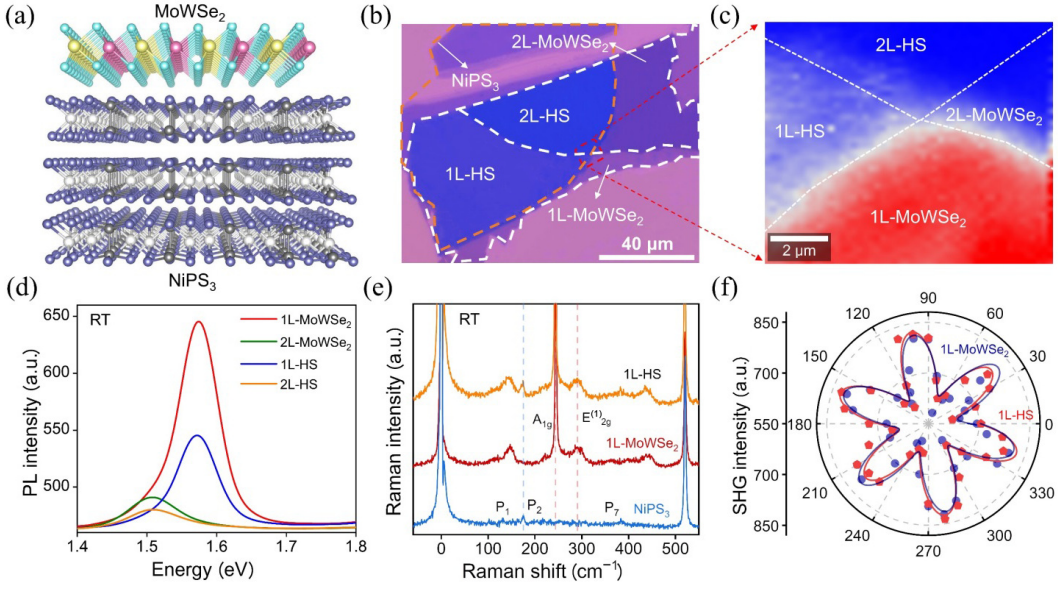

Figure 1 Optical characterization of the antiferromagnet-semiconductor vdW heterostructure at room temperature (RT). (a) Side view of the crystal structure of the $MoWSe_2/NiPS_3$ heterostructure. Different colored balls represent various atoms as follows: Ni (white), P (gray), S (slate blue), Mo (pink), W (yellow), and Se (cyan). (b) Optical image of $MoWSe_2/NiPS_3$ heterostructure on a SiO_2/Si substrate. The scale bar represents 40 μm. 1L-$MoWSe_2$ and 2L-$MoWSe_2$ refer to monolayer and bilayer $MoWSe_2$, respectively. Meanwhile, 1L-HS and 2L-HS denote heterostructures formed by monolayer and bilayer $MoWSe_2$ and few-layer $NiPS_3$. (c) PL mapping of the region enclosed by the red dashed box in (b). The scale bar is 2 μm. (d) PL spectra of 1L-$MoWSe_2$, 2L-$MoWSe_2$, 1L-HS and 2L-HS. (e) Raman spectra of 1L-$MoWSe_2$, few layer $NiPS_3$ and 1L-HS regions. (f) Polar plots of polarization-resolved SHG intensities in a parallel configuration, measured in 1L-$MoWSe_2$ and 1L-HS regions.

maximum in $MoWSe_2$ (see below Fig. 5), resulting in a band gap of 0.28 eV. This band alignment promotes interlayer charge transfer under laser excitation, leading to the pronounced quenching of the exciton peak in the PL spectrum of heterostructures [28, 34].

Figure 1(e) presents the Raman spectra of 1L-HS, 1L-$MoWSe_2$, and $NiPS_3$. The in-plane vibration mode P_2 of $NiPS_3$ appears at 175.4 cm^{-1}, while the typical in-plane $E^{(1)}_{2g}$ mode and out-of-plane A_{1g} mode of $MoWSe_2$ are observed at 292.4 and 247.7 cm^{-1}, consistent with previous studies [20, 32, 35]. These vibration modes are also present in the Raman spectrum of the $MoWSe_2/NiPS_3$ heterojunction, indicating strong coupling between two components [36]. To further investigate the symmetry of the $MoWSe_2/NiPS_3$, we measure the polarization-resolved second harmonic generation (SHG) emission signal with respect to laser analyzer polarization. For monolayer $MoWSe_2$ and 1L-HS, showing six-fold rotational symmetry in 1L-$MoWSe_2$, which is consistent with symmetry description of C_3 point group of non-centrosymmetric features. In contrast, the angle-resolved SHG pattern of the heterostructure reveals anisotropy, characterized by varying SHG intensities at local maxima (Fig. 1(f)). The emergence of an asymmetric SHG pattern in the $MoWSe_2/NiPS_3$ heterojunction suggests a modification of the lattice symmetry of the monolayer $MoWSe_2$ [37].

2.2 Emergence of anisotropy in $MoWSe_2/NiPS_3$

To illuminate the optical anisotropy induced by the $NiPS_3$ through heterointerface coupling, we conduct low-temperature spectroscopy measurements under non-resonant excitation conditions at 1.7 K. The PL spectrum of 1L-$MoWSe_2$ exhibits two emission peaks at energies of 1.647 and 1.621 eV, corresponding to neutral exciton (X_A) and charged exciton (X_T), respectively, with the PL intensity of X_T significantly exceeding that of X_A (Fig. 2(a)). In the $MoWSe_2/NiPS_3$ heterostructure, the neutral exciton (X^*_A) and charged exciton (X^*_T) appear at 1.658 and 1.627 eV, respectively. These excitonic states show a slight blue-shift compared to monolayer $MoWSe_2$, indicating the coupling between magnons in $NiPS_3$ and excitons in $MoWSe_2$ [38]. Additionally, the emission linewidth of $MoWSe_2$ excitons on $NiPS_3$ is slightly broader than those on SiO_2, likely due to the relaxation of photocarriers from $MoWSe_2$ layer to $NiPS_3$ layer.

Furthermore, temperature-dependent PL spectra of 1L-$MoWSe_2$ and 1L-HS show the typical temperature variation for neutral and charged excitons, as presented in Figs. S3(a) and S3(b) in the Electronic Supplementary Material (ESM). The solid lines fit the PL intensity of X^*_A and X^*_T using the following Eq. (1) [39]

$$I(T) = I(0)\left[1 + Ae^{-E_1/(k_B T)}\right] / \left[1 + Be^{-E_2/(k_B T)}\right] \quad (1)$$

where $I(0)$ represents the PL intensity at absolute zero (0 K). The parameters A and B are fitting constants, while k_B denotes the Boltzmann constant. E_1 corresponds to the activation energy that accounts for the increase in PL intensity with rising temperature, while E_2 denotes the activation energy associated with thermal quenching process at elevated temperatures. In addition, as the temperature rises, the energies of X^*_A and X^*_T undergo a redshift [29, 33, 40]. This shift can be precisely described by the following Eq. (2) [41]

$$E_g(T) = E_g(0) - S\langle\hbar w\rangle\left[\cosh\left(\langle\hbar w\rangle / 2k_B T\right) - 1\right] \quad (2)$$

where $E_g(0)$ and $E_g(T)$ represent the band gap energies at absolute zero and temperature T, respectively. S is dimensionless coupling parameter, while $\langle\hbar w\rangle$ denotes the average phonon energy. Additionally, k_B is the Boltzmann constant. This equation aligns with the temperature-dependent bandgap variation in semiconductors, as described by the Varshni equation [42].

To explore the anisotropic properties, measurements of polarization-resolved PL spectra are conducted. The polar plots of polarization-resolved PL intensity for monolayer $MoWSe_2$ and

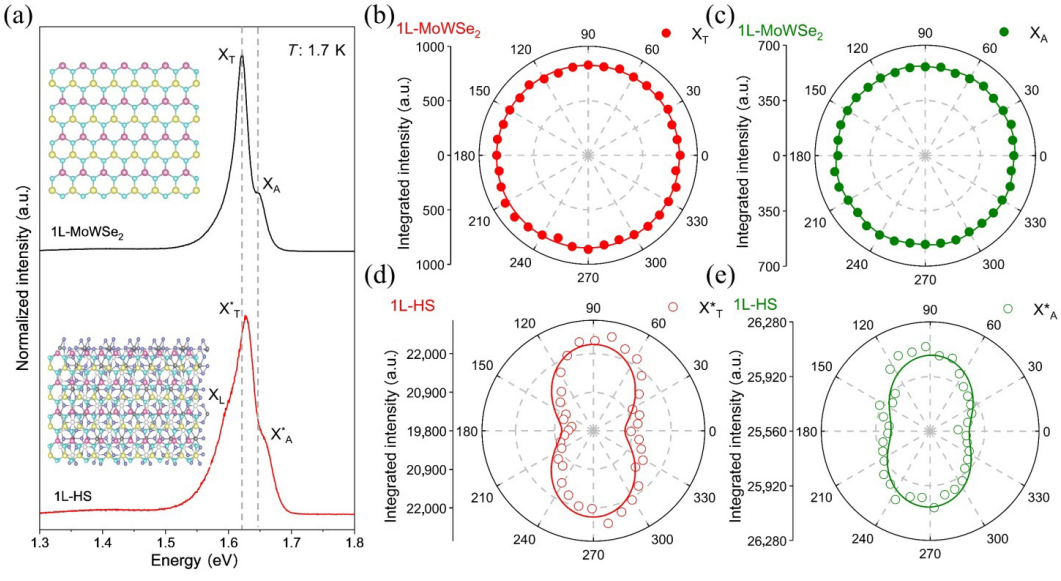

Figure 2 Anisotropic optical characteristics of monolayer $MoWSe_2$ and $MoWSe_2/NiPS_3$ heterostructure at cryogenic temperature with 532 nm laser excitation. (a) Normalized PL spectra of monolayer $MoWSe_2$ (black curve) and $MoWSe_2/NiPS_3$ heterostructure (red curve) at 1.7 K. Insets display crystal structure schematics of $MoWSe_2$ and $MoWSe_2/NiPS_3$. (b) and (c) Polarization-resolved PL integrated intensity polar plots of charged exciton X_T and neutral exciton X_A in 1L-$MoWSe_2$. Polarized PL spectra of intralayer excitons (X_T and X_A) show regular circle pattern. Polarization-resolved PL integrated intensity polar plots of (d) charged exciton X^*_T and (e) neutral exciton X^*_A in the $MoWSe_2/NiPS_3$ heterostructure. Polarized PL spectra of X^*_T and X^*_A displaying uneven two-lobed shapes. Circles and solid lines represent experimental and fitting data, respectively. X_T and X_A represent exciton emissions in 1L-$MoWSe_2$, while X^*_T and X^*_A denote exciton states in $MoWSe_2/NiPS_3$ heterostructure.

$MoWSe_2/NiPS_3$ are shown in Figs. 2(b)–2(f). X_T (X^*_T) and X_A (X^*_A) are represented by solid (hollow) red and green circles, respectively. The solid lines represent the fitting results of the experimental data using the following Eq. (3) [43]

$$I(\phi) = I_0 + I_p \cos^2(\phi - \phi_m) \quad (3)$$

where the fitting parameters, I_0, I_p, and ϕ_m denote the minimum PL intensity, the difference between maximum and minimum PL intensities, and the polarization angle corresponding to the maximum intensity, respectively. For intrinsic monolayer $MoWSe_2$, both X_T and X_A exhibit constant PL intensity as the laser polarization angle varies, displaying an almost uniformly circular pattern owing to its highly symmetric structure, indicating exciton isotropy in 1L-$MoWSe_2$ consistent with the characteristic of C_3 rotational symmetry of $MoWSe_2$ lattice (Figs. 2(b) and 2(c)). In stark contrast, the PL intensity of X^*_T and X^*_A in the $MoWSe_2/NiPS_3$ exhibits periodic variation as the rotation angle of the polarizer changes (Figs. 2(d) and 2(e)). The polarization-dependent PL intensity exhibits a 180° period, forming a dumbbell pattern, with the polarization angle oriented at 90° for polarized intralayer excitons. The anisotropy ratio, defined as

$$I_{max}/I_{min} = (I_0 + I_p)/I_0 \quad (4)$$

is 1.09 for X^*_T and 1.07 for X^*_A, respectively, indicating the emergence of anisotropy for $MoWSe_2$ induced by the low-symmetry $NiPS_3$ via heterointerface coupling. The formation of the $MoWSe_2/NiPS_3$ heterojunction breaks the C_3 rotational symmetry of $MoWSe_2$, leading to the optical anisotropy.

2.3 Manipulation of magnetic field on anisotropy

To further elucidate the anisotropy at $MoWSe_2/NiPS_3$ heterointerface, the polarization-dependent PL spectra of the heterostructure in the Faraday configuration are measured. Contour plots in Figs. 3(a)–3(i) visually depict the PL intensity of X^*_T as a function of polarization angle, with magnetic field sequentially decreasing from 9 to −9 T. When an external magnetic field is applied, the PL intensity of exciton emission varied with the laser polarization angle.

To investigate the effect of magnetism on linear polarization of $MoWSe_2/NiPS_3$, we analyze the polar plots of the polarized PL intensity for X^*_T and X^*_A across a variety of magnetic fields. These plots reveal anisotropic, dumbbell-shaped patterns (refer to Fig. 3(j) and Fig. S1 in the ESM). Notably, the angle between the excitation and emission polarization varies significantly with the magnetic field. At $B = 0$ T, the emission polarization aligns with the excitation direction. However, for $B \neq 0$ T, the emission polarization direction rotates relative to the excitation direction. In the presence of a positive magnetic field, as the strength increased from 0 to 9 T, the polarization angle rotates counterclockwise from 90° to 180°. Conversely, under a negative magnetic field, the polarization angle rotates clockwise from 90° to 0° as the field strength decreases from 0 to −9 T.

Using the polarization direction at 0 T as a reference, Fig. 3(k) illustrates the absolute deflection of the X^*_T polarization direction at various magnetic field strengths. This demonstrates that the deviation in polarization direction increases with magnetic field intensity. Previous studies have attributed such polarization angle deflection to valley coherence effects, where valley splitting leads to

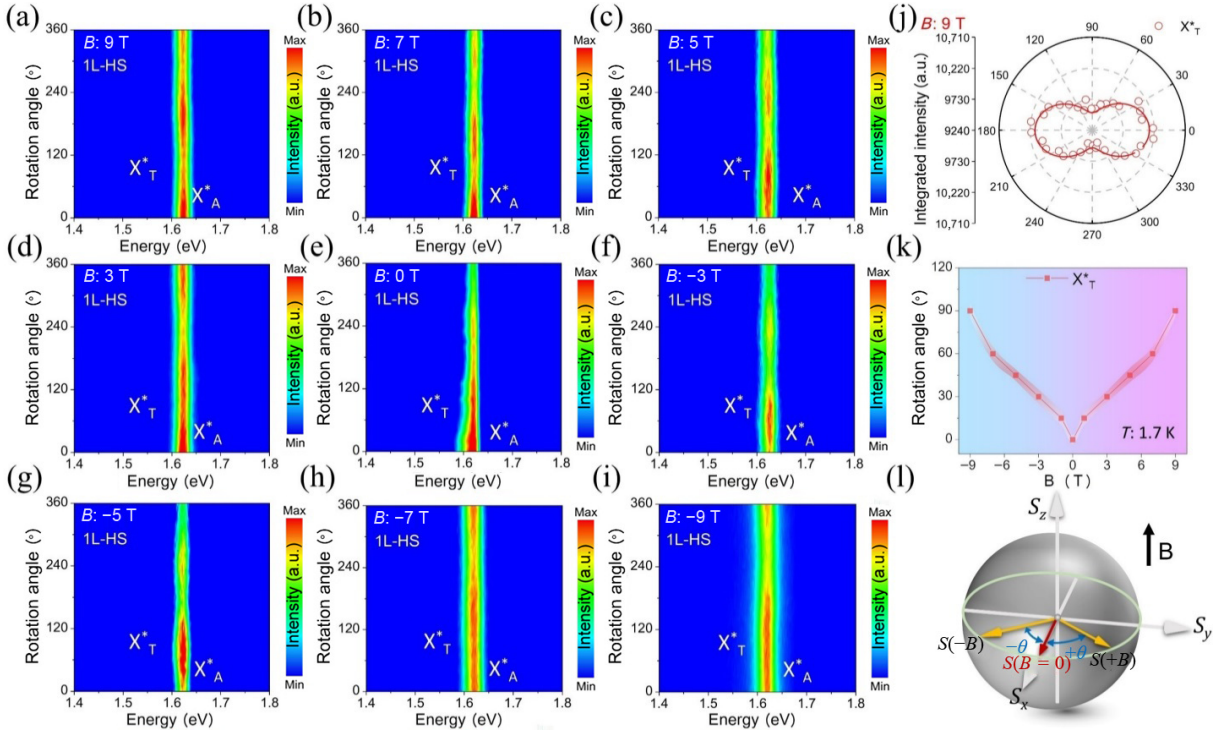

Figure 3 Magnetic field-dependent optical anisotropy at the $MoWSe_2/NiPS_3$ heterointerface. (a)–(d) Color plots showing polarization-resolved PL intensity for X^*_T and X^*_A as a function of photon energy under a positive magnetic field, varying from 9 to 3 T. (e) Color plot of polarization-resolved integrated PL intensity without out-of-plane magnetic field applied. (f)–(i) Color plots depicting polarization-resolved PL intensity for X^*_T and X^*_A as a function of photon energy under a negative magnetic field, ranging from −3 to −9 T, with a polarization angle of nearly 180°. (j) Polar plot of the PL intensity for peak X^*_T at 9 T, illustrating obvious polarization angle dependence. (k) The deflection angle (relative to the polarization direction at 0 T) as a function of the out-of-plane magnetic field, spanning from −9 to 9 T. (l) Depiction of valley coherent effect (exciton pseudospin) on the Bloch sphere. When $B = 0$ T, there is no rotation around the equatorial plane, as indicated by the red arrows.

variations in the superposition of valley coherence [44]. Analogous to spin, this coherent superposition of valley states can be represented by a vector on the equator of a Bloch sphere, as depicted in Fig. 3(l). The observed deflection direction under positive and negative magnetic fields aligns with this model. Notably, the polarization angles at ±9 and 0 T differ by nearly 90°, which is significantly larger than previous reported. In contrast, the deflection angles at 9 T for monolayer WSe_2 and WS_2 are approximately 25° and 20°, respectively, which are substantially smaller than the 90° observed in our results [45, 46]. Thus, valley coherence is not the sole contributor to the observed polarization deflection. Since $NiPS_3$ is a Néel-type antiferromagnetic material with Néel vector aligned along the a-axis, the antiferromagnetic order of $NiPS_3$ can significantly influence the anisotropic properties of $MoWSe_2/NiPS_3$ through strong heterointerface coupling [47]. When a vertical magnetic field is applied to the heterostructure, it alters the Néel vector, leading to a deflection in the polarization angle. Therefore, the deflection angle in $MoWSe_2/NiPS_3$ heterostructure under a magnetic field far exceeds that caused by valley coherence. Consequently, the deflection angle in the $MoWSe_2/NiPS_3$ heterostructure under a magnetic field exceeds what can be attributed solely to valley coherence. This substantial deflection suggests that the magnetic order in $NiPS_3$ also plays a significant role, which merits further investigation. Additionally, in the $MoWSe_2/NiPS_3$ heterostructure, valley splitting reaches approximately 5 meV with a *g*-factor of −9.3, and valley polarization increases with the magnetic field strength (Fig. S2 in the ESM).

Furthermore, Raman scattering spectra, which provide insights into phonon vibration modes, are sensitive to structural anisotropy. The interface coupling between $MoWSe_2$ and $NiPS_3$ also induces anisotropic behavior in Raman modes. To gain a deeper understanding of Raman intensity anisotropy, we use a Raman tensor to analyze and fit the polarized Raman intensity. The Raman intensity is typically represented by the following Eq. (5) [48]

$$I \propto \left| \vec{e_i} \cdot \vec{R} \cdot \vec{e_s} \right|^2 \quad (5)$$

where $e_i = (\sin\theta, 0, \cos\theta)$ represents the unit vectors of the polarization directions of the incident light, $e_s = (\sin\theta, 0, \cos\theta)$ and $e_s = (-\cos\theta, 0, \sin\theta)$ represent scattered light in parallel and perpendicular configurations, respectively, and R indicates the Raman tensor associated with symmetric modes [49]. Angle-dependent polarized Raman spectra of $MoWSe_2/NiPS_3$ are measured at low temperatures, with and without applying magnetic field, as shown in Fig. 4. The polar plots of polarized Raman intensity of out-of-plane A_{1g} mode at 247.7 cm^{-1} are presented in Figs. 4(a)–4(c). As the laser analyzer angle rotates, the intensity of the A_{1g} mode exhibits periodic variations with a 180° period, yielding a two-lobed shape. This phenomenon indicates significant anisotropy generated in the $MoWSe_2/NiPS_3$ interface, as shown in contour plots of polarized Raman spectra in Figs. 4(d)–4(f). Polarization-resolved Raman spectra of monolayer $MoWSe_2$ are provided in Fig. S4 in the ESM, showing apparent isotropy. Moreover, when a magnetic field is applied, a noticeable rotation in the polarization direction is observed. Relative to the initial laser polarization (90°) at zero magnetic field, a positive 9 T magnetic field causes the polarization to rotate counterclockwise by approximately 35°. Conversely, a negative 9 T magnetic field results in a clockwise rotation clockwise rotation of about 34°. The modulation mechanism of the out-of-plane magnetic field on the polarization direction of the A_{1g} mode resembles that observed in polarized PL. This phenomenon can be attributed to both valley coherence and as antiferromagnetic ordering in $NiPS_3$.

2.4 Theoretical calculations unveiling the origin of anisotropy

To gain the origin of the optical anisotropy induced by the interface effect in an antiferromagnet/TMDC heterostructures, we conduct DFT calculations using the projector-augmented wave (PAW)

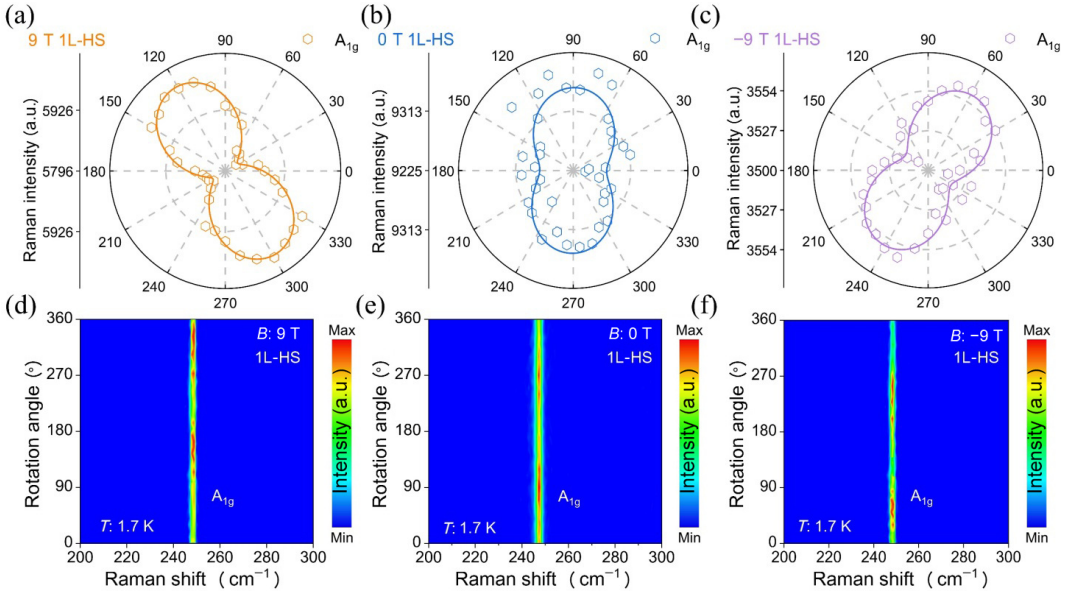

Figure 4 Angle-resolved Raman spectra of the $MoWSe_2/NiPS_3$ heterolayer measured in the parallel configuration under varying magnetic fields. (a) Polar plot showing the Raman intensity of the out-of-plane A_{1g} mode located at 247.7 cm^{-1} under a positive magnetic field of 9 T. The polarization angle related to maximum polarized intensity is 125°. (b) Polarization angle-dependent Raman intensity of A_{1g} mode in the absence of a magnetic field, with a polarization angle of 90°. (c) Polar plot displaying integrated intensity of A_{1g} mode under a −9 T magnetic field, displaying a polarization angle of 56°. When a positive magnetic field is applied, the polarization direction rotates counterclockwise, whereas with a negative magnetic field, it deflects clockwise. Color maps depicting the integrated Raman scattering intensities at the $MoWSe_2/NiPS_3$ heterointerface under a magnetic field of (d) 9, (e) 0, and (f) −9 T, respectively.

method. For simplicity, we focus on the band structure and charge distributions at the conduction and valence band edges of a 1L $MoWSe_2$/1L $NiPS_3$ heterostructure. The DFT-computed band structures and corresponding density of states (DOS) are illustrated in Figs. 5(a) and 5(b), respectively. The lowest conduction band edge is primarily contributed by Ni and S atoms in the $NiPS_3$ layer, while the highest valence band edge is contributed by Mo and W atoms in the $MoWSe_2$ layer, indicating a type-II band alignment. This alignment leads to a significant reduction in PL intensity due to charge transfer from $MoWSe_2$ to $NiPS_3$ upon laser excitation.

The charge distributions at the band edges of the conduction and valence bands for the $MoWSe_2$/$NiPS_3$ heterostructure are shown in Figs. 5(c)–5(k). Here, Figs. 5(c), 5(f) and 5(i) display side views along the *a*-axis direction of the three-dimensional (3D) charge density distribution at the Γ point of the valence band, the Γ and K points of the conduction band, respectively. Figures 5(d), 5(g) and 5(j) depict charge density distributions along the *c*-axis direction. It is evident that the charge density of both the conduction and valence bands is concentrated near the localized potential fields of Mo and W atoms in the $MoWSe_2$ layer. We extract 2D charge density distributions from the 3D crystal structure along the (001) plane, as shown in Figs. 5(e), 5(h) and 5(k). The red and blue contour lines represent the maximum and minimum charge densities, respectively. Figures 5(e) and 5(h) reveal that the charge density distribution at the high-symmetry points in the Brillouin zone is spatially uniform. In contrast, Fig. 5(k) shows a spatially non-uniform charge density distribution in the conduction band at the K point, decreasing gradually from the center to the edges. This non-

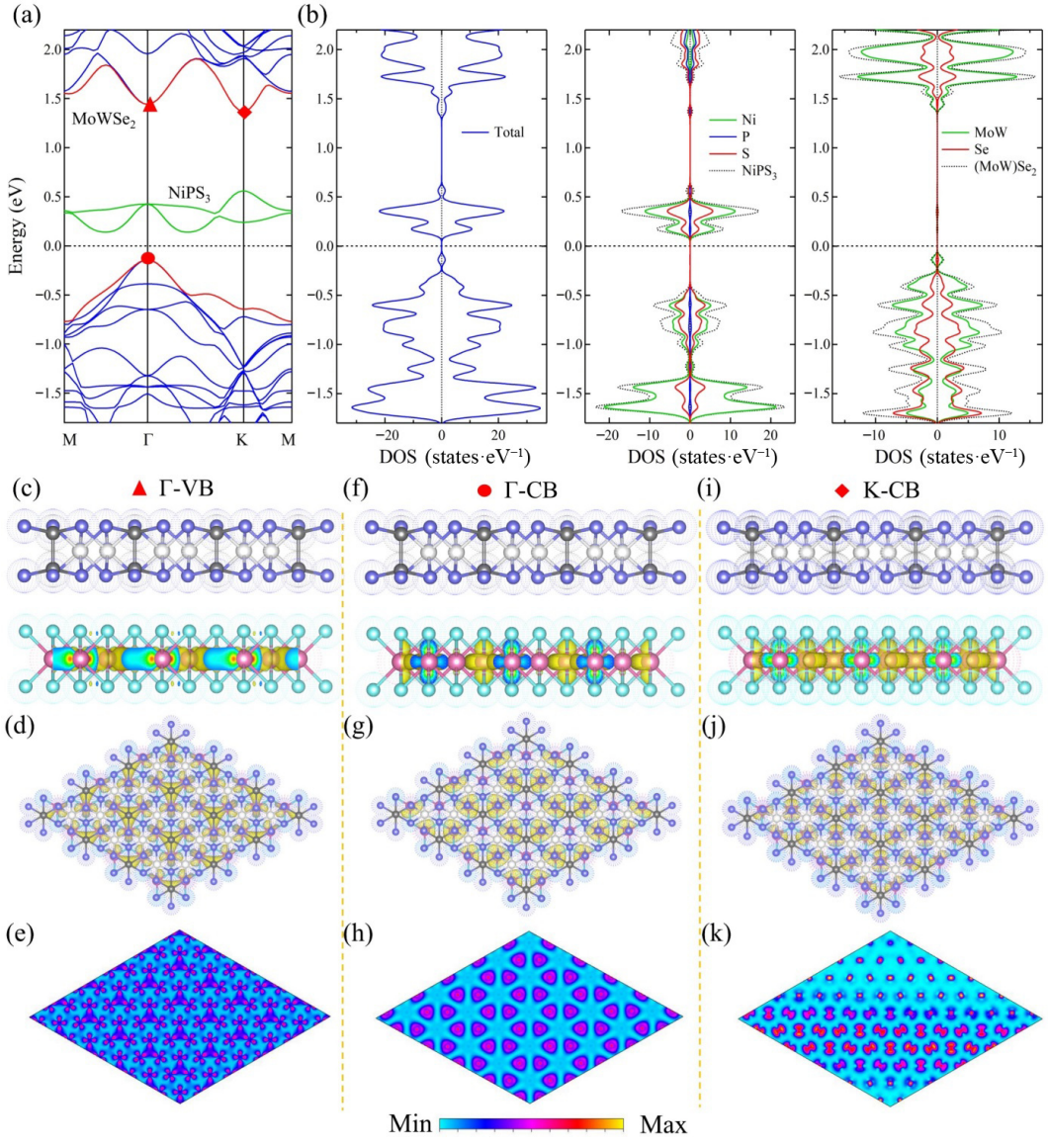

Figure 5 Electronic structure and charge distribution in $MoWSe_2$/$NiPS_3$. (a) DFT calculation of the energy band structure for $MoWSe_2$/$NiPS_3$. The Fermi level is set to zero, as indicated by the dashed horizontal line. (b) Calculated DOS for $MoWSe_2$/$NiPS_3$, 1L-$NiPS_3$, and 1L-$MoWSe_2$, shown from left to right. Three-dimensional (c) side view and (d) top view of the valence band edge charge distribution along the *a*-axis at the Γ point, with electron localization predominantly in the $MoWSe_2$ layer. (f) Side view and (g) top view of the conduction band edge charge distribution along the *a*-axis at the Γ-point, with electrons localized in the $MoWSe_2$ layer. (i) Side view and (j) top view of the conduction band edge charge distribution along the *a*-axis at the K point, with electrons localized in the $MoWSe_2$ layer. Two-dimensional profiles of the electron density distribution in the $MoWSe_2$ layer at three points, the isosurface values are (e) 0.004, (h) 0.004, and (k) 0.006 e·Å^{-3}, respectively. The color bar represents variations from minimum to maximum charge density.

uniformity is attributed to the symmetry-breaking effect of $NiPS_3$ on $MoWSe_2$, which modulates the lattice distortion of the $MoWSe_2$ atomic structures at the band edges. These findings provide strong evidence supporting the observed optical anisotropy in the $MoWSe_2/NiPS_3$ heterostructure.

3 Conclusion

In summary, we have successfully constructed anisotropic/isotropic interface within $MoWSe_2/NiPS_3$ heterostructure. Polarization-dependent spectroscopy measurements at low temperatures reveal a strong polarization dependence in both PL and Raman scattering, indicating a notable optical anisotropy in the $MoWSe_2/NiPS_3$ heterostructure. This anisotropy is highly responsive to magnetic fields, with a substantial polarization deflection of 90° observed at 9 T. Such significant deviation in polarization angle is ascribed to both valley coherent effects and the antiferromagnetic ordering in $NiPS_3$. Furthermore, DFT calculations pinpoint the origin of the optical anisotropy at the $MoWSe_2/NiPS_3$ interface to spatially non-uniform charge density distribution near the conduction band edge of $MoWSe_2$. The pronounced polarization properties and tunable polarization angle under external magnetic fields highlight the potential of $MoWSe_2/NiPS_3$ heterostructures for applications in polarized photodetectors, light modulators, and magneto-optical modulation devices, paving the way for innovative advancements in these technologies.

4 Methods

4.1 Sample fabrication

$MoWSe_2$ and $NiPS_3$ flakes were mechanically exfoliated from bulk crystals (HQ Graphene) using a gold-assisted method [50, 51], onto SiO_2/Si wafers. The thickness of the flakes was determined through optical techniques and PL spectral analysis. $MoWSe_2/NiPS_3$ heterojunctions were assembled on SiO_2/Si substrates via layer-by-layer stacking, using the PDMS/PC dry transfer method, and facilitated by a custom-built three-dimensional transfer platform. All fabrication steps were performed in a glove box to prevent sample degradation. Afterward, the samples were annealed at 150 °C in a high vacuum (argon environment) for 3 h to remove surface contaminants and enhance interface adhesion.

4.2 Optical measurements

Room temperature PL measurements were performed using a confocal Raman system (WITec Alpha 300R) with a 50× objective lens. Micro-photoluminescence spectra at cryogenic temperatures were obtained using a WITec Cryo Raman system equipped with a 70× microscope objective. The samples were mounted on an *x-y-z* pressure platform and cooled to 1.7 K within a cryostat filled with liquid helium. The sample temperature was precisely controlled using a closed-loop cryostat (autocube Systems, attoDRY2100). A magnetic field of up to 9 T was applied using a resistance magnet in Faraday configuration. The polarization of the PL and Raman spectra was analyzed using a half wave plate and a linear polarizer.

4.3 DFT calculation

DFT calculations were performed using the Vienna *ab initio* simulation package (VASP) [52] with the all-electron PAW method [53]. The Perdew–Burke–Ernzerhof (PBE) generalized gradient approximation revised for solids (PBEsol-GGA) [54] was used to assess structural and magnetic stability. Supercells of 1L-$(Mo_{0.5}W_{0.5})Se_2$/1L-$NiPS_3$, with a 20 Å thick vacuum layer, were employed to simulate the zigzag and Néel-type antiferromagnetic (AFM) states in the $NiPS_3$ monolayer [55] , using *C*2/*m* (No. 12) and *P*31*m* (No. 157) symmetries. Valence states for Ni ($4s^13d^9$), Mo ($5s^14d^5$), W ($6s^15d^5$), P ($3s^23p^3$), S ($3s^23p^4$), and Se ($4s^24p^4$) were utilized, with an energy cutoff of 500 eV for the plane wave basis set. The virtual crystal approximation (VCA) was used for the mixed $Mo_{0.5}W_{0.5}$ form. Electronic band structures and density of states were computed using the modified Becke-Johnson (mBJ) functional [56]. Convergence criteria for electronic self-consistent and ionic relaxations were set to 10^{-6} eV and 0.01 eV·Å^{-1}, respectively.

Electronic Supplementary Material: Supplementary material (magnetic field dependence of neutral and charged excitons at the $MoWSe_2/NiPS_3$ interface, effects of the magnetic field on valley polarization and Zeeman splitting, temperature-dependent PL spectra, and polar plots depicting the anisotropic Raman scattering intensity of 1L-$MoWSe_2$) is available in the online version of this article at https://doi.org/10.26599/NR.2025.94907111.

Data availability

All data needed to support the conclusions in the paper are presented in the manuscript and the Electronic Supplementary Material. Additional data related to this paper may be requested from the corresponding author upon request.

Acknowledgements

The authors gratefully acknowledge the essential support provided by the National Natural Science Foundation of China (No. 52373311). Additional significant contributions are made by the High-Performance Complex Manufacturing Key State Laboratory Project at Central South University (No. ZZYJKT2020-12) and the Key Project of the Natural Science Program of the Xinjiang Uygur Autonomous Region (No. 2023D01D03). Special thanks are extended to the Australian Research Council for its crucial role in advancing this research (ARC Discovery Project, DP180102976). J.-T. Wang also acknowledges support from the Strategic Priority Research Program of the Chinese Academy of Sciences (No. XDB33000000), the National Natural Science Foundation of China (Nos. 92263202 and 12374020), and the National Key Research and Development Program of China (No. 2020YFA0711502). This work is further supported by the Innovation Program for Quantum Science and Technology (No. 2021ZD0301605). The authors also express their sincere appreciation to the High-Performance Computing Center of Central South University for providing critical computing resources for this study.

Declaration of competing interest

All the contributing authors report no conflict of interests in this work.

Author contributions

The project management and design were led by Y. P. L. M. X. G. and X. X. were responsible for device fabrication and characterization, including Raman and PL techniques. X. X. conducted the low-temperature measurements, while J. Y. C., Z. W.

L., Y. P. L., J. N. D., J. H., and F. P. O. Y. contributed to data interpretation. Theoretical calculations and related explanations, based on DFT, were provided by J.-T. W. The initial draft of the paper was prepared by Y. P. L., X. X., and Z. W. L., with all authors actively participating in manuscript revisions and contributing as needed.

Use of AI statement

None.

References

[1] Du, L. J.; Hasan, T.; Castellanos-Gomez, A.; Liu, G. B.; Yao, Y. G.; Lau, C. N.; Sun, Z. P. Engineering symmetry breaking in 2D layered materials. *Nat. Rev. Phys.* **2021**, *3*, 193–206.

[2] Du, L. J.; Tang, J.; Liang, J.; Liao, M. Z.; Jia, Z. Y.; Zhang, Q. H.; Zhao, Y. C.; Yang, R.; Shi, D. X.; Gu, L. et al. Giant valley coherence at room temperature in 3R WS_2 with broken inversion symmetry. *Research (Wash D C)* **2019**, *2019*, 6494565.

[3] Finney, N. R.; Yankowitz, M.; Muraleetharan, L.; Watanabe, K.; Taniguchi, T.; Dean, C. R.; Hone, J. Tunable crystal symmetry in graphene-boron nitride heterostructures with coexisting moiré superlattices. *Nat. Nanotechnol.* **2019**, *14*, 1029–1034.

[4] Velasco, J.; Jing, L.; Bao, W.; Lee, Y.; Kratz, P.; Aji, V.; Bockrath, M.; Lau, C. N.; Varma, C.; Stillwell, R. et al. Transport spectroscopy of symmetry-broken insulating states in bilayer graphene. *Nat. Nanotechnol.* **2012**, *7*, 156–160.

[5] Zhang, W. X.; Huang, Z. S.; Zhang, W. L.; Li, Y. R. Two-dimensional semiconductors with possible high room temperature mobility. *Nano Res.* **2014**, *7*, 1731–1737.

[6] Zhang, Y. J.; Kamiya, K.; Yamamoto, T.; Sakano, M.; Yang, X. H.; Masubuchi, S.; Okazaki, S.; Shinokita, K.; Chen, T. M.; Aso, K. et al. Symmetry engineering in twisted bilayer WTe_2. *Nano Lett.* **2023**, *23*, 9280–9286.

[7] Q.; Ray, E. L.; Song, T. C.; Taniguchi, T.; Watanabe, K.; McGuire, M. A.; Xiao, D.; Xu, X. D. Tuning inelastic light scattering via symmetry control in the two-dimensional magnet CrI_3. *Nat. Nanotechnol.* **2020**, *15*, 212–216.

[8] Geim, A. K.; Grigorieva, I. V. Van der Waals heterostructures. *Nature* **2013**, *499*, 419–425.

[9] Li, Z. Y.; Huang, J. W.; Zhou, L.; Xu, Z. A.; Qin, F.; Chen, P.; Sun, X. J.; Liu, G.; Sui, C.; Qiu, C. Y. et al. An anisotropic van der Waals dielectric for symmetry engineering in functionalized heterointerfaces. *Nat. Communi.* **2023**, *14*, 5568.

[10] Neupane, G. P.; Zhou, K.; Chen, S. S.; Yildirim, T.; Zhang, P. X.; Lu, Y. P. In-plane isotropic/anisotropic 2D van der Waals Heterostructures for Future Devices. *Small* **2019**, *15*, 1804733.

[11] X.; Yang, Y. H.; Wu, M. H.; Hu, C. G.; Shen, W. F.; Gong, Y. J.; Huang, L.; Jiang, C. B.; Zhang, Y. Z.; Ajayan, P. M. Highly in-plane optical and electrical anisotropy of 2D germanium arsenide. *Adv. Funct. Mater.* **2018**, *28*, 1707379.

[12] Xu, X. Z.; Liu, C.; Sun, Z. H.; Cao, T.; Zhang, Z. H.; Wang, E. G.; Liu, Z. F.; Liu, K. H. Interfacial engineering in graphene bandgap. *Chem. Soc. Rev.* **2018**, *47*, 3059–3099.

[13] Usman, A.; Adel Aly, M.; Masenda, H.; Thompson, J. J. P.; Gunasekera, S. M.; Mucha-Kruczyński, M.; Brem, S.; Malic, E.; Koch, M. Enhanced excitonic features in an anisotropic ReS_2/WSe_2 heterostructure. *Nanoscale* **2022**, *14*, 10851–10861.

[14] X.; Hao, H.; Kang, Y.; Liu, Q. R.; Sui, Y.; Wei, K.; Cheng, X. A.; Jiang, T. Distinctive interfacial charge behavior and versatile photoresponse performance in isotropic/anisotropic WS_2/ReS_2 heterojunctions. *ACS Appl. Mater. Interfaces* **2020**, *12*, 53475–53483.

[15] Zhao, M.; Zhang, W. T.; Liu, M. M.; Zou, C.; Yang, K. Q.; Yang, Y.; Dong, Y. Q.; Zhang, L. J.; Huang, S. M. Interlayer coupling in anisotropic/isotropic van der Waals heterostructures of ReS_2 and MoS_2 monolayers. *Nano Res.* **2016**, *9*, 3772–3780.

[16] Li, X. Z.; Jones, A. C.; Choi, J.; Zhao, H.; Chandrasekaran, V.; Pettes, M. T.; Piryatinski, A.; Tschudin, M. A.; Reiser, P.; Broadway, D. A. et al. Proximity-induced chiral quantum light generation in strain-engineered $WSe_2/NiPS_3$ heterostructures. *Nat. Mater.* **2023**, *22*, 1311–1316.

[17] Ramos, M.; Marques-Moros, F.; Esteras, D. L.; Mañas-Valero, S.; Henríquez-Guerra, E.; Gadea, M.; Baldoví, J. J.; Canet-Ferrer, J.; Coronado, E.; Calvo, M. R. Photoluminescence enhancement by band alignment engineering in $MoS_2/FePS_3$ van der Waals heterostructures. *ACS Appl. Mater. Interfaces* **2022**, *14*, 33482–33490.

[18] M.; Wei, Y. H.; Zhang, X. Z.; Wei, Z. H.; Luo, W.; Guo, X.; Liu, J.; Peng, G.; Cai, W. W.; Huang, H. et al. Symmetry engineering induced in-plane polarization in MoS_2 through van der Waals interlayer coupling. *Adv. Funct. Mater.* **2022**, *32*, 2202658.

[19] Lee, J. U.; Lee, S.; Ryoo, J. H.; Kang, S.; Kim, T. Y.; Kim, P.; Park, C. H.; Park, J. G.; Cheong, H. Ising-type magnetic ordering in atomically thin $FePS_3$. *Nano Lett.* **2016**, *16*, 7433–7438.

[20] Kim, K.; Lim, S. Y.; Lee, J. U.; Lee, S.; Kim, T. Y.; Park, K.; Jeon, G. S.; Park, C. H.; Park, J. G.; Cheong, H. Suppression of magnetic ordering in XXZ-type antiferromagnetic monolayer $NiPS_3$. *Nat. Communi.* **2019**, *10*, 345.

[21] Yang, S. X.; Hu, C. G.; Wu, M. H.; Shen, W. F.; Tongay, S.; Wu, K. D.; Wei, B.; Sun, Z. Y.; Jiang, C. B.; Huang, L. et al. In-plane optical anisotropy and linear dichroism in low-symmetry layered TlSe. *ACS Nano* **2018**, *12*, 8798–8807.

[22] Mehlawat, K.; Alfonsov, A.; Selter, S.; Shemerliuk, Y.; Aswartham, S.; Büchner, B.; Kataev, V. Low-energy excitations and magnetic anisotropy of the layered van der Waals antiferromagnet $Ni_2P_2S_3$. *Phys. Rev. B* **2022**, *105*, 214427.

[23] Tongay, S.; Narang, D. S.; Kang, J.; Fan, W.; Ko, C.; Luce, A. V.; Wang, K. X.; Suh, J.; Patel, K. D.; Pathak, V. M. et al. Two-dimensional semiconductor alloys: Monolayer $Mo_{1-x}W_xSe_2$. *Appl. Phys. Lett.* **2014**, *104*, 012101.

[24] Komsa, H. P.; Krasheninnikov, A. V. Two-dimensional transition metal dichalcogenide alloys: Stability and electronic properties. *J. Phys. Chem. Lett.* **2012**, *3*, 3652–3656.

[25] Akamatsu, T.; Ideue, T.; Zhou, L.; Dong, Y.; Kitamura, S.; Yoshii, M.; Yang, D. Y.; Onga, M.; Nakagawa, Y.; Watanabe, K. et al. A van der Waals interface that creates in-plane polarization and a spontaneous photovoltaic effect. *Science* **2021**, *372*, 68–72.

[26] Li, X. R.; Xie, X.; Wu, B.; Chen, J. Y.; Li, S. F.; He, J.; Liu, Z. W.; Wang, J. T.; Liu, Y. P. Observation of robust anisotropy in WS_2/BP heterostructures. *Nano Res.* **2024**, *17*, 6749–6756.

[27] Xie, X.; Wu, B.; Ding, J. N.; Li, S. F.; Chen, J. Y.; He, J.; Liu, Z. W.; Wang, J. T.; Liu, Y. P. Emergence of optical anisotropy in moiré superlattice via heterointerface engineering. *Nano Lett.* **2024**, *24*, 9186–9194.

[28] Wu, B.; Zheng, H. H.; Li, S. F.; Wang, C. T.; Ding, J. N.; He, J.; Liu, Z. W.; Wang, J. T.; Liu, Y. P. Effect of layered-coupling in twisted WSe_2 moiré superlattices. *Nano Res.* **2023**, *16*, 3435–3442.

[29] Zheng, H. H.; Wu, B.; Li, S. F.; He, J.; Chen, K. Q.; Liu, Z. W.; Liu, Y. P. Evidence for interlayer coupling and moiré excitons in twisted WS_2/WS_2 homostructure superlattices. *Nano Res.* **2023**, *16*, 3429–3434.

[30] Li, S. F.; Zheng, H. H.; Ding, J. N.; Wu, B.; He, J.; Liu, Z. W.; Liu, Y. P. Dynamic control of moiré potential in twisted WS_2–WSe_2 heterostructures. *Nano Res.* **2022**, *15*, 7688–7694.

[31] Zhong, J. H.; Wu, B.; Madoune, Y.; Wang, Y. P.; Liu, Z. W.; Liu, Y. P. $PdSe_2/MoSe_2$ vertical heterojunction for self-powered photodetector with high performance. *Nano Res.* **2022**, *15*, 2489–2496.

[32] C. T.; Neumann, M.; Balamurugan, K.; Park, H. J.; Kang, S.; Shiu, H.

W.; Kang, J. H.; Hong, B. H.; Han, M.; Noh, T. W. et al. Exfoliation and Raman spectroscopic fingerprint of few-layer $NiPS_3$ van der Waals crystals. *Sci. Rep.* **2016**, *6*, 20904.

[33] Wu, B.; Wang, Y. P.; Zhong, J. H.; Zeng, C.; Madoune, Y.; Zhu, W. T.; Liu, Z. W.; Liu, Y. P. Observation of double indirect interlayer exciton in $MoSe_2/WSe_2$ heterostructure. *Nano Res.* **2022**, *15*, 2661–2666.

[34] Wu, B.; Zheng, H. H.; Ding, J. N.; Wang, Y. P.; Liu, Z. W.; Liu, Y. P. Observation of interlayer excitons in trilayer type-II transition metal dichalcogenide heterostructures. *Nano Res.* **2022**, *15*, 9588–9594.

[35] Zhang, M.; Wu, J. X.; Zhu, Y. M.; Dumcenco, D. O.; Hong, J. H.; Mao, N. N.; Deng, S. B.; Chen, Y. F.; Yang, Y. L.; Jin, C. H. et al. Two-dimensional molybdenum tungsten diselenide alloys: Photoluminescence, Raman scattering, and electrical transport. *ACS Nano* **2014**, *8*, 7130–7137.

[36] Kunstmann, J.; Mooshammer, F.; Nagler, P.; Chaves, A.; Stein, F.; Paradiso, N.; Plechinger, G.; Strunk, C.; Schüller, C.; Seifert, G. et al. Momentum-space indirect interlayer excitons in transition-metal dichalcogenide van der Waals heterostructures. *Nat. Phys.* **2018**, *14*, 801–805.

[37] Liang, J.; Zhang, J.; Li, Z. Z.; Hong, H.; Wang, J. H.; Zhang, Z. H.; Zhou, X.; Qiao, R. X.; Xu, J. Y.; Gao, P. et al. Monitoring local strain vector in atomic-layered $MoSe_2$ by second-harmonic generation. *Nano Lett.* **2017**, *17*, 7539–7543.

[38] Dang, J. C.; Yang, M. W.; Xie, X.; Yang, Z.; Dai, D. J.; Zuo, Z. C.; Wang, C.; Jin, K. J.; Xu, X. L. Enhanced valley polarization in $WS_2/LaMnO_3$ heterostructure. *Small* **2022**, *18*, 2106029.

[39] Huang, J. N.; Hoang, T. B.; Mikkelsen, M. H. Probing the origin of excitonic states in monolayer WSe_2. *Sci. Rep.* **2016**, *6*, 22414.

[40] Fang, Y. T.; Wang, L.; Sun, Q. L.; Lu, T. P.; Deng, Z.; Ma, Z. G.; Jiang, Y.; Jia, H. Q.; Wang, W. X.; Zhou, J. M. et al. Investigation of temperature-dependent photoluminescence in multi-quantum wells. *Sci. Rep.* **2015**, *5*, 12718.

[41] Ross, J. S.; Wu, S. F.; Yu, H. Y.; Ghimire, N. J.; Jones, A. M.; Aivazian, G.; Yan, J. Q.; Mandrus, D. G.; Xiao, D.; Yao, W. et al. Electrical control of neutral and charged excitons in a monolayer semiconductor. *Nat. Communi.* **2013**, *4*, 1474.

[42] Tongay, S.; Zhou, J.; Ataca, C.; Lo, K.; Matthews, T. S.; Li, J. B.; Grossman, J. C.; Wu, J. Q. Thermally driven crossover from indirect toward direct bandgap in 2D semiconductors: $MoSe_2$ versus MoS_2. *Nano Lett.* **2012**, *12*, 5576–5580.

[43] Hu, B. Q.; Xie, X.; Ouyang, X. Y.; Chen, J. Y.; Li, S. F.; He, J.; Liu, Z. W.; Wang, J. T.; Liu, Y. P. Unveiling optical anisotropy in disrupted symmetry WSe_2/SiP heterostructures. *Nano Res.* **2024**, *17*, 8585–8591.

[44] Wang, G.; Marie, X.; Liu, B. L.; Amand, T.; Robert, C.; Cadiz, F.; Renucci, P.; Urbaszek, B. Control of exciton valley coherence in transition metal dichalcogenide monolayers. *Phys. Rev. Lett.* **2016**, *117*, 187401.

[45] Nagler, P.; Ballottin, M. V.; Mitioglu, A. A.; Durnev, M. V.; Taniguchi, T.; Watanabe, K.; Chernikov, A.; Schüller, C.; Glazov, M. M.; Christianen, P. C. M. et al. Zeeman splitting and inverted polarization of biexciton emission in monolayer WS_2. *Phys. Rev. Lett.* **2018**, *121*, 057402.

[46] Schmidt, R.; Arora, A.; Plechinger, G.; Nagler, P.; del Águila, A. G.; Ballottin, M. V.; Christianen, P. C. M.; de Vasconcellos, S. M.; Schüller, C.; Korn, T. et al. Magnetic-field-induced rotation of polarized light emission from monolayer WS_2. *Phys. Rev. Lett.* **2016**, *117*, 077402.

[47] Wu, B.; Zheng, H. H.; Li, S. F.; Ding, J. N.; He, J.; Liu, Z. W.; Liu, Y. P. Enhanced interlayer neutral excitons and trions in $MoSe_2/MoS_2/MoSe_2$ trilayer heterostructure. *Nano Res.* **2022**, *15*, 5640–5645.

[48] Li, X.; Liu, H. Y.; Ke, C. M.; Tang, W. Q.; Liu, M. Y.; Huang, F. H.; Wu, Y. P.; Wu, Z. M.; Kang, J. Y. Review of anisotropic 2D materials: Controlled growth, optical anisotropy modulation, and photonic applications. *Laser Photonics Rev.* **2021**, *15*, 2100322.

[49] Li, L.; Han, W.; Pi, L. J.; Niu, P.; Han, J. B.; Wang, C. L.; Su, B.; Li, H. Q.; Xiong, J.; Bando, Y. et al. Emerging in-plane anisotropic two-dimensional materials. *InfoMat* **2019**, *1*, 54–73.

[50] Huang, Y.; Pan, Y. H.; Yang, R.; Bao, L. H.; Meng, L.; Luo, H. L.; Cai, Y. Q.; Liu, G. D.; Zhao, W. J.; Zhou, Z. et al. Universal mechanical exfoliation of large-area 2D crystals. *Nat. Communi.* **2020**, *11*, 2453.

[51] Huang, Y.; Sutter, E.; Shi, N. N.; Zheng, J. B.; Yang, T. Z.; Englund, D.; Gao, H. J.; Sutter, P. Reliable exfoliation of large-area high-quality flakes of graphene and other two-dimensional materials. *ACS Nano* **2015**, *9*, 10612–10620.

[52] Kresse, G.; Furthmüller, J. Efficient iterative schemes for *ab initio* total-energy calculations using a plane-wave basis set. *Phys. Rev. B* **1996**, *54*, 11169–11186.

[53] Blöchl, P. E. Projector augmented-wave method. *Phys. Rev. B* **1994**, *50*, 17953–17979.

[54] Perdew, J. P.; Ruzsinszky, A.; Csonka, G. I.; Vydrov, O. A.; Scuseria, G. E.; Constantin, L. A.; Zhou, X. L.; Burke, K. Restoring the density-gradient expansion for exchange in solids and surfaces. *Phys. Rev. Lett.* **2008**, *100*, 136406.

[55] Gu, Y. H.; Zhang, Q.; Le, C. C.; Li, Y. X.; Xiang, T.; Hu, J. P. Ni-based transition metal trichalcogenide monolayer: A strongly correlated quadruple-layer graphene. *Phys. Rev. B* **2019**, *100*, 165405.

[56] Becke, A. D.; Johnson, E. R. A simple effective potential for exchange. *J. Chem. Phys.* **2006**, *124*, 221101.